JGR Oceans

RESEARCH ARTICLE
10.1029/2023JC020391

Key Points:

- Locations of frontal activity in the Hauraki Gulf (HG) directly relate to wind direction and bathymetric features
- El Niño Southern Oscillation phases contribute to fine-scale frontal dynamics, limiting connectivity between sub-parts of the HG during *El Niño* and enhancing it during *La Niña*

Supporting Information:

Supporting Information may be found in the online version of this article.

Correspondence to:
A. Della Penna,
alice.penna@auckland.ac.nz

Citation:
Lhériau-Nice, A., & Della Penna, A. (2024). Variability of fine-scale chlorophyll fronts in the Tīkapa Moana Te Moananui ā Toi Hauraki Gulf, Aotearoa New Zealand. *Journal of Geophysical Research: Oceans*, *129*, e2023JC020391. https://doi.org/10.1029/2023JC020391

Received 28 AUG 2023
Accepted 25 JAN 2024
Corrected 11 MAR 2024

This article was corrected on 11 MAR 2024. See the end of the full text for details.

Author Contributions:
Conceptualization: Alexandre Lhériau-Nice, Alice Della Penna
Data curation: Alexandre Lhériau-Nice
Formal analysis: Alexandre Lhériau-Nice
Investigation: Alexandre Lhériau-Nice, Alice Della Penna
Methodology: Alexandre Lhériau-Nice, Alice Della Penna
Resources: Alexandre Lhériau-Nice
Software: Alexandre Lhériau-Nice
Supervision: Alice Della Penna
Validation: Alice Della Penna
Visualization: Alexandre Lhériau-Nice, Alice Della Penna

Variability of Fine-Scale Chlorophyll Fronts in the Tīkapa Moana Te Moananui ā Toi Hauraki Gulf, Aotearoa New Zealand

Alexandre Lhériau-Nice[1] and **Alice Della Penna**[1,2]

[1]Te Whare Takiura Mātai Pūtaiao Moana Institute of Marine Science, Waipapa Taumata Rau University of Auckland, Tāmaki Makaurau Auckland, Aotearoa New Zealand, [2]Te Kura Mātauranga Koiora School of Biological Sciences, Waipapa Taumata Rau University of Auckland, Tāmaki Makaurau Auckland, Aotearoa New Zealand

Abstract Aotearoa New Zealand's marine environment is heavily impacted by El Niño Southern Oscillation (ENSO). Little is known about the effect of ENSO on oceanographic properties in the area or their consequences on the distribution of marine organisms. Here we characterize the spatio-temporal variability of fine-scale fronts (<10 km) in the area of the Tīkapa Moana Te Moananui ā Toi Hauraki Gulf (HG) and investigate how it is impacted by dominant wind direction, seasonality, and ENSO phase. We processed satellite Ocean-Land Color Instrument images from 2016 to 2022 with a fit-for-purpose version of the Belkin and O'Reilly frontal detection algorithm. We find coherent shifts in the position of fine-scale features depending on the ENSO phase, with *El Niño* isolating the gulf sub-regions and *La Niña* connecting them together. Overall, fronts tend to co-locate with the 70 and 40 m isobaths in the outer and inner HG respectively, and their locations shift close or away from shore in response to changes in dominant wind direction. Furthermore, offshore frontal occurrences increase during winter and spring, and nearshore ones increase during summer and autumn. Our results sketch a first assessment of the distribution of fine-scale features in a biologically important yet understudied region.

Plain Language Summary Fine-scale fronts are small oceanic features less than 10 km in size where water masses of different origins meet. They play a key role in structuring the distribution of marine organisms. Here, we investigate their impact on marine microalgae and water color in the Tīkapa Moana Te Moananui ā Toi Hauraki Gulf (HG). We use satellite images and a specialized algorithm to detect and relate the distribution of fronts with seasons, dominant wind direction, and ENSO phase (*El Niño* vs. *La Niña*). El Niño Southern Oscillation phases play a role in the region, causing the fronts to alternately separate (during *El Niño*) and connect (during *La Niña*) different parts of the Gulf. We also find that fronts are more frequent offshore during winter and spring and nearshore during summer and autumn. The distribution of these fine-scale fronts is closely linked to wind patterns and underwater topography, particularly the 70 m isobath outside the Gulf and the 40 m isobath. Overall, this research provides insights into the spatio-temporal variability of fine-scale fronts in the HG and highlights potential shifts in ecologically relevant regions.

1. Introduction

Fronts are regions where water masses having different origins and physical properties (e.g., temperature, salinity, nutrient concentration) meet. They are ubiquitous in open ocean and coastal regions. The properties of fronts associated with boundary currents such as the East Australian Current, Gulf Stream, and Kuroshio Current have been documented for decades (Palter, 2015; Ridgway & Hill, 2009; Su, 1987). Recent modeling and observations suggest that fine-scale features such as mesoscale (50–100 km, a week to month; McGillicuddy, 2016) and submesoscale (≈1 km, few days; Thomas et al., 2008) play a key role in structuring the distribution of tracers, including biologically relevant ones. For example, submesoscale structures can be associated with strong vertical velocities, increased phytoplankton abundance, changes in phytoplankton community composition, and estimated carbon export as documented by Mangolte et al. (2023) and in the work reviewed by Lévy et al. (2012) and Mahadevan (2016).

Home to about 1.6 million people in Tāmaki Makaurau Auckland (the largest city in Aotearoa New Zealand) alone, the Tīkapa Moana Te Moananui ā Toi Hauraki Gulf (HG) is under the stewardship of 19 iwi (Māori tribes) authorities recognized by the Auckland Council (2021). The HG is an enclosed body of water connected to the

Writing – original draft:
Alexandre Lhériau-Nice
Writing – review & editing:
Alexandre Lhériau-Nice, Alice Della Penna

ocean by three channels: the Jellicoe, Cradock, and Colville channels, respectively between the islands of Te-Hauturu-ō-Toi (Little Barrier), Aotea (Great Barrier) and the Coromandel Peninsula (Cape Colville, Figure 1). The dominant oceanic current in the region is the East Auckland Current (EAuC), which originates from the East Australian Current (Stevens et al., 2021) and flows from north-west (NW) to south-east (SE) following the east coast of Aotearoa. Because of the shape of the coast, winds with a component along the NW-SE axis have a strong impact on the region (Zeldis et al., 2004). Said winds contribute to the seasonal succession of the plankton communities by switching from westerlies dominance in spring to easterlies in late summer (Zeldis et al., 2004; Zeldis & Willis, 2015). This is reflected by larger diatoms in spring replaced with dinoflagellates and nanoflagellates in late summer (Chang et al., 2003). However, while there is a broad understanding of the general circulation of the HG, there is no description of the frontal patterns at the submesoscale nor observations of the effect of fronts and associated patchiness on primary productivity, larval dispersal, or foraging grounds for megafauna.

Our aim is to identify the typical spatial patterns in frontal distribution with relation to seasons and inter-annual variability related to El Niño Southern Oscillation (ENSO), which has been suggested to be a key driver in the atmospheric and marine conditions in the HG (Zeldis et al., 2004). We hypothesize a significant difference in location of surface chlorophyll fronts between winter-spring and summer-autumn (Chang et al., 2003), as well as surface fronts being more intense and closer to shore during NW winds (Zeldis et al., 2004).

Fronts are commonly studied using satellite sea surface temperature, because it has been publicly accessible since the 1970's (Smith et al., 1970). Consequently, a number of front detection methods from satellite imaging rely primarily on temperature (Cayula & Cornillon, 1992; Mauzole et al., 2020), or are adapted from temperature (Liu & Levine, 2016; Miller, 2004). As we focus on the effect of fronts on the biology of the HG, like the plankton shift observed by Chang et al. (2003), we chose to use ocean color as a proxy for chlorophyll and abundance of phytoplankton in the water. Ocean color fronts, by contrast to temperature fronts, do not only occur when two water mass of different optical properties meet, but can also be generated by phytoplankton blooms on the front's edge (*active fronts*), characterized by higher chlorophyll concentration (Belkin & O'Reilly, 2009; Lévy et al., 2018).

We characterized the distribution of <10 km surface fronts in the HG region and investigated their temporal variability by relying on the assumptions there after. First, chlorophyll is a more suited proxy than temperature to identify fronts with a biological signature (Lévy et al., 2018). Second, fronts (i.e., chlorophyll) can be detected using the Belkin and O'Reilly Algorithm (BOA) (Belkin & O'Reilly, 2009). Third, the variability of submesoscale structures will change the position of plankton patches in time (Chang et al., 2003), affecting the ocean color. Fourth, said variability contribution to front patterns can be analyzed in season/wind/ENSO phase composites.

We used the Ocean and Land Color Instrument (OLCI) at 300 m spatial resolution, and optimized the Belkin and O'Reilly Algorithm (BOA; Belkin & O'Reilly, 2009) for our study area (Figure 1). We then segregated data from 2016 to 2022 (the period for which the 300 m product is available) depending on the corresponding season, dominant wind direction from a local weather station or ENSO phase. Maps were then statistically compared using the method from Levine et al. (2009). This allowed us to identify the factors that significantly contribute to the HG frontal dynamic and to highlight areas where chlorophyll fronts are likely to occur.

We find that almost all selected factors (winds, season, ENSO) affect the distribution of fronts, with most of the frontal patterns being traced back to wind direction and bathymetry. The observed ocean color patterns also match known geographical subregions of the Gulf.

2. Methods

2.1. High Resolution Ocean Color Data

The data used in this study are Ocean and Land Color Instrument (OLCI) images taken from the mission Sentinel 3-A and B, and provided by the Copernicus Marine Service under product ID *009_103* (Copernicus, 2016). This data product combines ocean color, chlorophyll concentration and turbidity measured by sensors on the satellites Sentinel-3A and 3B (Colella et al., 2022; Copernicus, 2016) and is available as daily maps at 300 m spatial resolution starting from 25 May 2016. We compiled 6.5 years of OLCI 300 m resolution maps starting from 25 May 2016 to 31 December 2022.

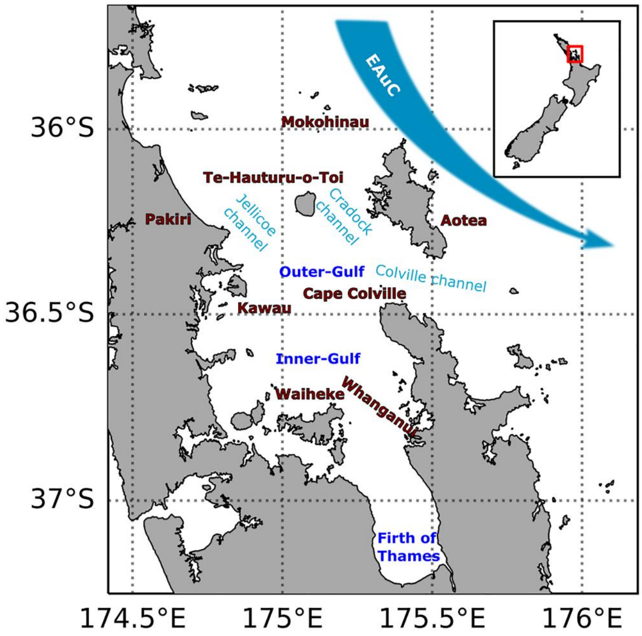

Figure 1. Map of the Tīkapa Moana Te Moananui ā Toi Hauraki Gulf.

Even though we will refer to any frontal structures simply as "fronts" in this article, it is important to note that our analysis is focused on fronts detectable from near-surface chlorophyll observations (Colella et al., 2022). This means that the sub-surface expression of the fronts, which can account for a significant part of productivity is not detected in our approach, despite these subsurface expressions being relatively common in the offshore waters of North-East of Aotearoa New-Zealand (Chiswell et al., 2022). However, considering that most of our study area is relatively shallow (<100 m) and weakly stratified with frequent surface to bottom mixing, we do not expect this limitation to greatly impact our study (Paul, 1968). Further studies are required to investigate the vertical structure of the detected features and how it may vary depending on seasonal and inter-annual drivers.

2.2. Surface Front Detection

Before processing the images, we removed all values superior to 30 mg.m^{-3} and applied a log function of the chlorophyll (CHL) values as per Copernicus recommendation (EUMETSAT, 2021).

Chlorophyll fronts mostly occur in two situations: when water masses of different optical properties meet creating a 2-population structure, and when the phytoplankton community from one water mass benefit from the nutrient from another (and potentially from the supply of nutrients brought to the surface by vertical water movements), resulting in phytoplankton blooms on the front's edge, creating a 3-population structure. Both result in an area with a chlorophyll gradient although the second occurrence appears as a chlorophyll filament (see Figure 4 in Belkin and O'Reilly (2009)) rather than step-like gradient as for temperature fronts (Cayula & Cornillon, 1992). For this reason, we adapted the algorithm from Belkin and O'Reilly (2009), which is designed to detect ridge fronts and step-like ones, to our study site.

This fit-for-purpose version of the BOA algorithm (Belkin & O'Reilly, 2009; Galuardi, 2012; Lin et al., 2019), thereafter pyBOA, has a number of modifications and additions (Figure 2). The first modification from the original BOA algorithm is the identification of local extrema. While the original algorithm (Belkin & O'Reilly, 2009; Lin et al., 2019) uses a slicing method on the $5 * 5$ window, effectively masking 8 out of the 25 values from a given window, in this study we used an approach similar to Galuardi (2012) which lets the algorithm consider all 25 values of a window. In practice, this allows a better identification of the local CHL extrema in each $5 * 5$ pixels window before applying a median filter on a $3 * 3$ pixels window. Following the median filter, a Sobel edge detection method was used, corrected to take into account the distance distortion using the haversine formula. In addition, we included a cloud and land proximity filter to avoid artifacts created by being in the vicinity of an empty cell (here 4 pixels or ≈1.2 km), and we defined a rolling window of $64 * 64$ pixels for front thresholding enabling detection nearshore as well as offshore. This means that the pixels near land were removed, and the threshold was determined as the local 90th percentile (similarly to Lehahn et al. (2007)), allowing it to vary spatially rather than be constant. Experimenting with other window sizes (e.g., $16 * 16$ and $32 * 32$) suggested that $64 * 64$ is the optimal size window for our study region as it maximizes delineation and minimizes artifacts.

Finally, the areas flagged by the 90th percentile threshold were cleaned using two iterations of morphological thinning (from group to line keeping the central shape), spur removal (to eliminate terminal pixels) and artifact removal with features less than 7 pixels long considered artifacts, including a cross-shaped dilation and holes removal in-between both iterations. Removing features smaller than 7 pixels mitigated the impact of artifacts from the smaller kernel of the pyBOA ($3 * 3$).

2.3. Group Segregation by Wind Direction, Season, and ENSO Phase

Upon detection, each valid pixel from OLCI images was saved in binary form with 1 being the *front* category and 0 the *non-front*. Different groups were then formed based on one of the subsequent criteria: dominant wind direction (eight groups), season (four groups), ENSO phase (three groups). The dominant wind direction was calculated on a daily basis using the hourly data of the Mokohinau islands station (Figure 1) from Meteorological

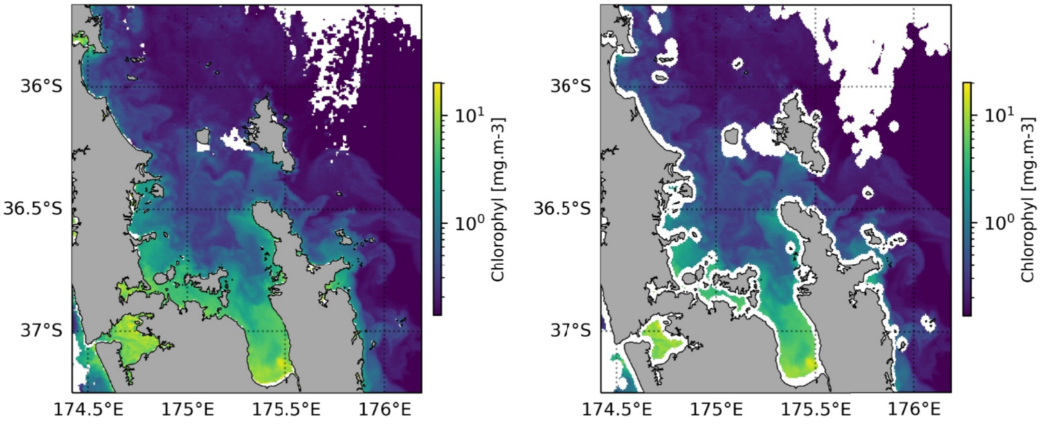

(a) Raw CHL from Copernicus (2016)   (b) Land and cloud proximity exclusion

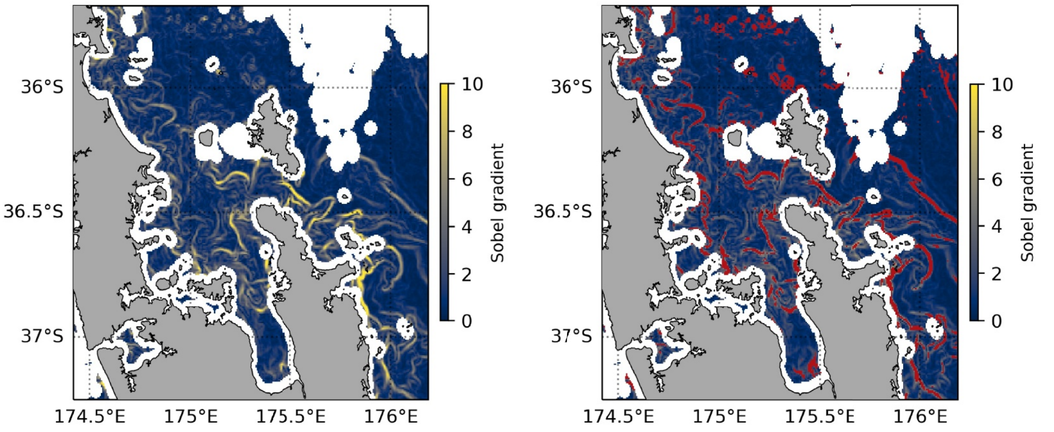

(c) Sobel gradient   (d) Selected front areas in red

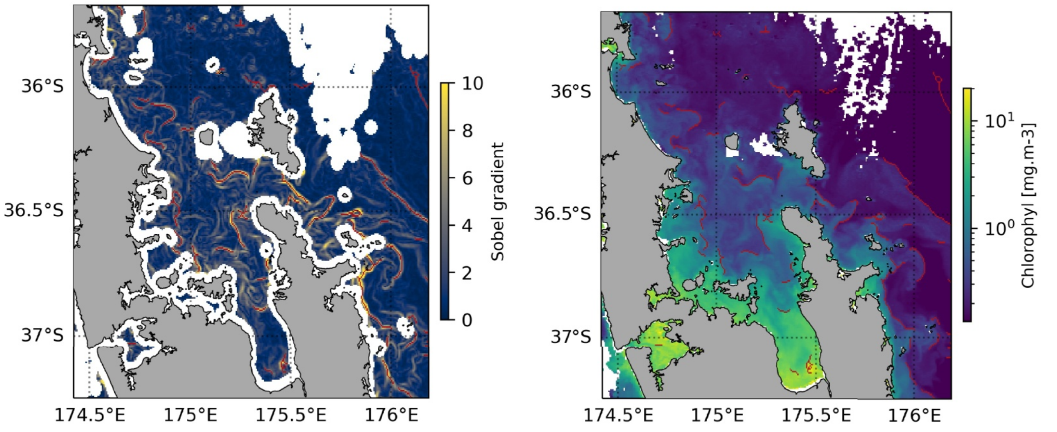

(e) Morphological thinning to lines   (f) Overlap of the front lines with the CHL

Figure 2. Panel showing the process followed by the pyBOA.

Service of New Zealand Ltd and separated between the four cardinals (North, South, East, West) and four subcomponents (North-West, NW; South-West, SW; South-East, SE; North-East, NE). The Mokohinau islands weather station was chosen as it is located reasonably far from land. We assessed how different observations from

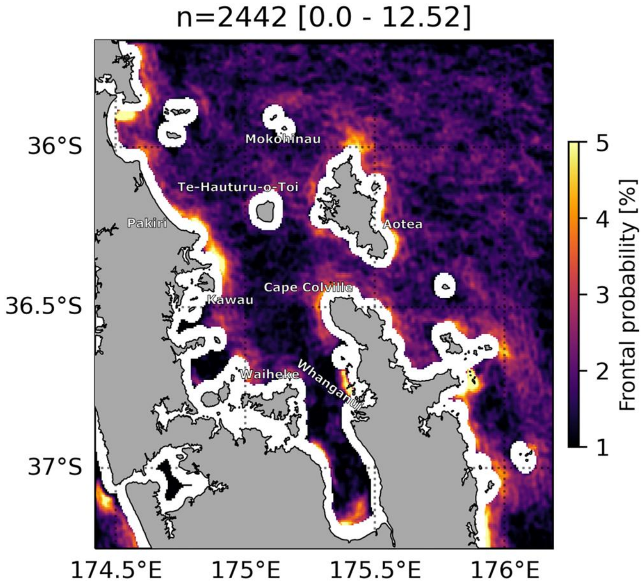

Figure 3. Probability map in the Tīkapa Moana Te Moananui ā Toi Hauraki Gulf.

this station are from those measured in another HG weather station, as well as those from the ECMWF reanalysis ERA5 (Hersbach et al., 2023). The results of our analysis can be found in Supporting Information S1. The period covering September–November was classified as spring; December–February as summer; March–May as autumn; June–August as winter. The Southern Oscillation Index (SOI) provided by NOAA (2022) was used to determine the state of the ENSO oscillation like so: $SOI < -0.5$, *El Niño*; $-0.5 \leq SOI \leq 0.5$, Neutral; $0.5 < SOI$, *La Niña*. Upon segregation, each binary file was passed through a low-pass filter with a $5 * 5$ Gaussian kernel accounting for finer-scale variability (e.g., tides; Hu et al. (2016)) and detection errors. The resulting map was then normalized in order to keep the original *front* category value equal to 1. By doing so, we considered all pixel as potential fronts, the higher values near 1 being more likely as they were detected by the pyBOA, and the lower values near 0 less likely and, as said prior, impacted by tides or detection errors. The results were aggregated using the *Pf* from Equation 1 to produce single factor frontal probability maps (see Figure 3):

$$Pf(i) = \frac{\sum_1^n front\ category_i}{\sum_1^n non - empty\ values_i} \tag{1}$$

where i is a given pixel and n the number of days considered.

2.4. Statistical Analysis

Prior to any statistical analysis, we pooled data from 2,442 days following Equation 1. This resulted in one probability map showing the probability of detecting surface fronts over 2,442 days (Figure 3), as well as probability maps based on individual environmental variables (Figures 4, 5, and 7), with each corresponding group (wind, season, ENSO; Table S1 in Supporting Information S1).

To compare maps, we used the statistical approach described by Levine et al. (2009). The idea behind this approach (*jackknife*) is that by removing one factor (e.g., winter if we are considering a seasonal study), it is possible to evaluate the impact of said factor on the overall map. For each factor, we created a jackknife map by removing the days associated with that factor from the full data set (front and valid pixels alike) as seen in Equation 2:

$$J(A) = \frac{Pf(all) - Pf(A)}{V(all) - V(A)} \tag{2}$$

where $Pf(all)$ is the probability of observing a front for a pixel in the full data set, $Pf(A)$ the probability of observing a front for a pixel in the group A, $V(all)$ the number of non-empty observations for 1 pixel in the full data set, $V(A)$ the number of non-empty observations for 1 pixel in the group A (which might be a given season, ENSO phase, etc.). Each $J(A)$ was then transformed using Equation 3 into a δ map. The ENSO calculation was done differently as the SOI includes a *Neutral* factor which we considered as the norm in this analysis. Hence, the $J(A)$ step was skipped and all ENSO factors were treated using a simple delta of probability using Equation 4.

$$\delta(A) = J(A) - Pf(all) \tag{3}$$

$$\delta(A) = Pf(A) - Pf(Neutral) \tag{4}$$

where A is a given factor.

This process created $n = 12$ jackknife maps (four seasons, eight wind orientations) and $n = 14$ δ maps (adding two SOI) of identical dimensions ($285 * 318$ pixels), transformed into single column table of 90,630 lines for statistical analysis.

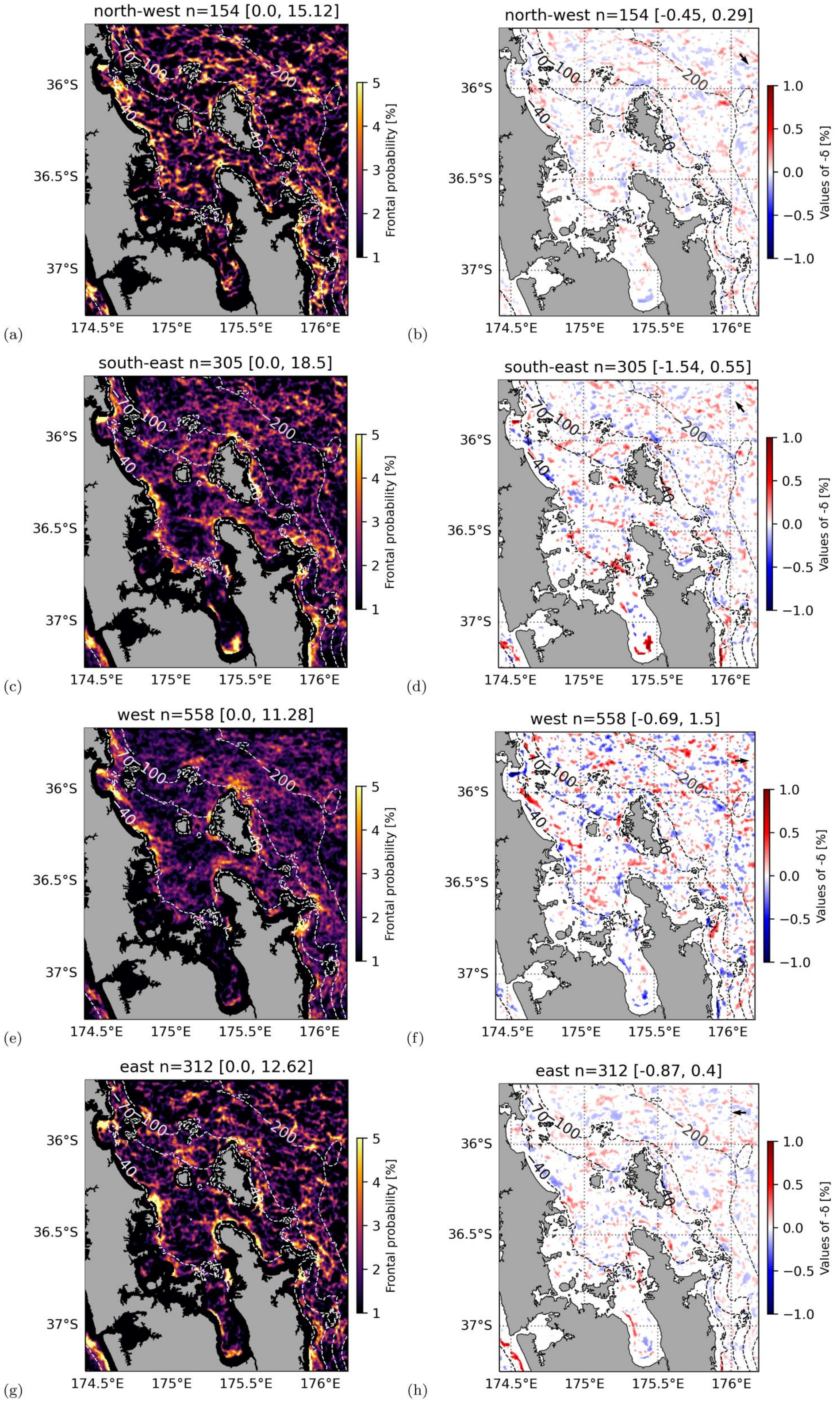

north-west n=154 [0.0, 15.12]

north-west n=154 [-0.45, 0.29]

(a) (b)

south-east n=305 [0.0, 18.5]

south-east n=305 [-1.54, 0.55]

(c) (d)

west n=558 [0.0, 11.28]

west n=558 [-0.69, 1.5]

(e) (f)

east n=312 [0.0, 12.62]

east n=312 [-0.87, 0.4]

(g) (h)

Figure 4. Probability maps and values of $-\delta$ outside of the 75th percentile confidence interval based on wind orientation, top to bottom: North-West (a, b), South-East (c, d), West (e, f), East (g, h). Probabilities are on the left column (a, c, e, g) and δ on the right. Dashed line indicates 40, 70, 100, and 200 m depth. The title of each sub-figure indicates the factor, *n* the number of days and the min and max values. Wind orientation arrow displayed in δ maps top-right corner.

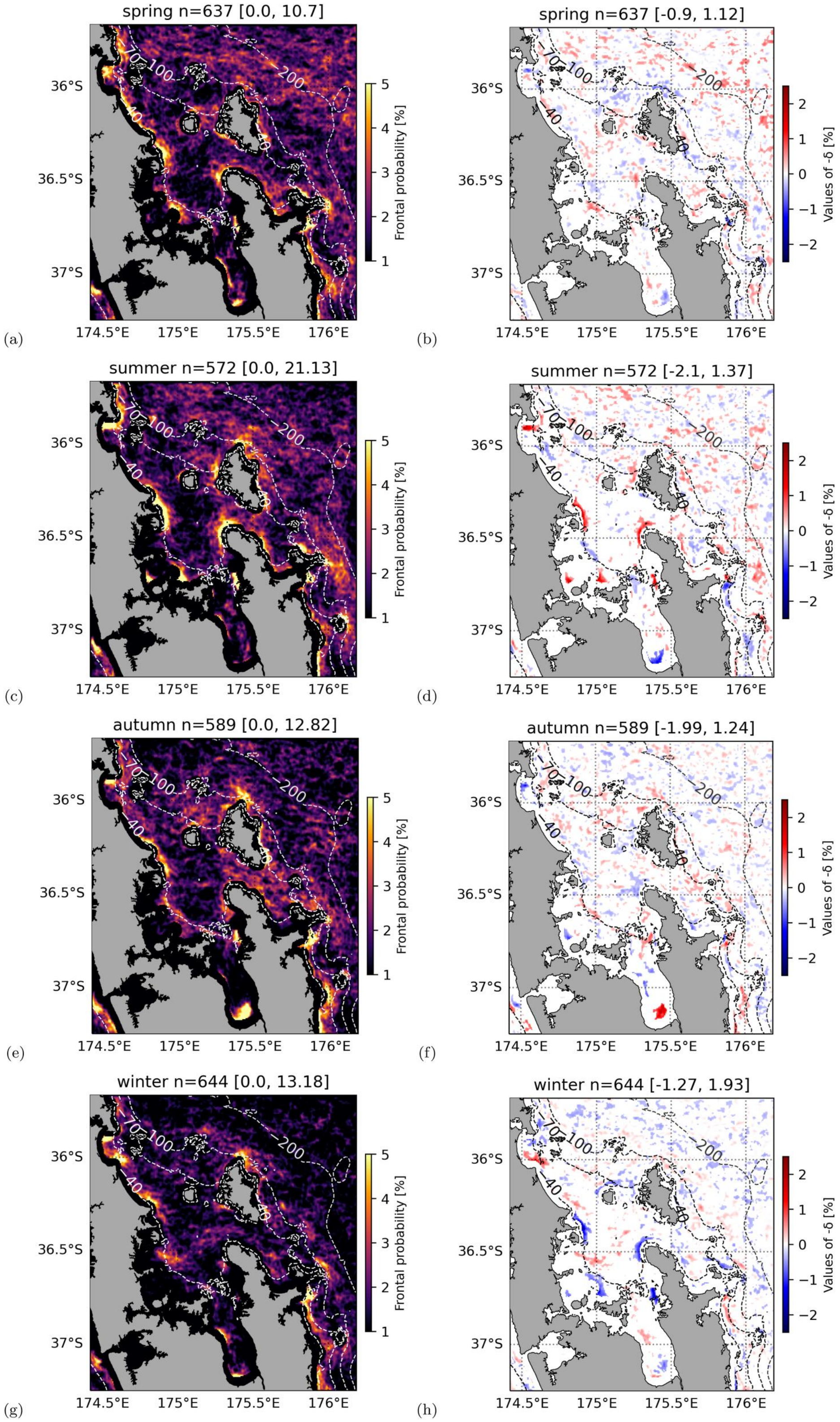

Figure 5. Probability maps and values of $-\delta$ outside of the 75th percentile confidence interval during seasons, top to bottom: spring (a, b), summer (c, d), autumn (e, f), winter (g, h). Probabilities are on the left column (a, c, e, g) and δ on the right. Dashed lines indicate 40, 70, 100, and 200 m depth. The title of each sub-figure indicates the factor, n the number of days and the min and max values. Note the change of scale in δ.

Table 1
Summary of Bootstrap t-Test Analysis of Jackknifes Maps Highlighting Major Contribution of Wind Orientation, Season, and El Niño Southern Oscillation Phase

Factor	Mean	σ	Min	1st Q	Median	3rd Q	Max	Student t	Mean Δ	*p*-value	CI inferior	CI superior
Spring	1.7387	0.7529	0	1.29	1.61	2.01	13.25	72.69	$6.32 \cdot 10^{-4}$	<0.01	$6.22 \cdot 10^{-4}$	$6.42 \cdot 10^{-4}$
Summer	1.7508	0.6984	0	1.34	1.64	2.01	11.82	49.82	$5.11 \cdot 10^{-4}$	<0.01	$4.99 \cdot 10^{-4}$	$5.22 \cdot 10^{-4}$
Autumn	1.8030	0.7224	0	1.38	1.69	2.08	12.71	−1.29	$-1.15 \cdot 10^{-5}$	0.211	$-2.20 \cdot 10^{-5}$	$-1.46 \cdot 10^{-6}$
Winter	1.9076	0.7656	0	1.46	1.80	2.18	12.54	−120.88	$-1.06 \cdot 10^{-3}$	<0.01	$-1.07 \cdot 10^{-3}$	$-1.05 \cdot 10^{-3}$
El Niño SOI	1.7595	0.8509	0	1.20	1.64	2.16	11.87	18.30	$4.24 \cdot 10^{-4}$	<0.01	$3.97 \cdot 10^{-4}$	$4.51 \cdot 10^{-4}$
La Niña SOI	1.7907	0.8179	0	1.28	1.67	2.12	12.72	6.52	$1.12 \cdot 10^{-4}$	<0.01	$9.20 \cdot 10^{-5}$	$1.32 \cdot 10^{-4}$
North	1.8019	0.7051	0	1.39	1.69	2.05	12.52	−0.34	$-1.02 \cdot 10^{-7}$	0.747	$-4.38 \cdot 10^{-7}$	$2.38 \cdot 10^{-7}$
North.East	1.8027	0.7051	0	1.40	1.69	2.05	12.49	−4.39	$-7.86 \cdot 10^{-6}$	<0.01	$-9.92 \cdot 10^{-6}$	$-5.78 \cdot 10^{-6}$
East	1.8077	0.7041	0	1.40	1.70	2.06	12.77	−15.93	$-5.78 \cdot 10^{-5}$	<0.01	$-6.20 \cdot 10^{-5}$	$-5.37 \cdot 10^{-5}$
South.East	1.7915	0.7000	0	1.38	1.68	2.04	12.86	19.52	$1.03 \cdot 10^{-4}$	<0.01	$9.75 \cdot 10^{-5}$	$1.10 \cdot 10^{-4}$
South	1.7924	0.7031	0	1.38	1.68	2.06	12.36	15.95	$9.47 \cdot 10^{-5}$	<0.01	$8.78 \cdot 10^{-5}$	$1.02 \cdot 10^{-4}$
South.West	1.8125	0.7399	0	1.37	1.70	2.08	12.12	−14.04	$-1.07 \cdot 10^{-4}$	<0.01	$-1.16 \cdot 10^{-4}$	$-9.80 \cdot 10^{-5}$
West	1.8065	0.7445	0	1.37	1.69	2.07	12.75	−7.06	$-4.62 \cdot 10^{-5}$	<0.01	$-5.40 \cdot 10^{-5}$	$-3.88 \cdot 10^{-5}$
North.West	1.8022	0.7119	0	1.39	1.69	2.05	12.45	−1.07	$-3.18 \cdot 10^{-6}$	0.277	$-6.56 \cdot 10^{-6}$	$2.93 \cdot 10^{-7}$

Note. Factors resulting in non-significant *p*-values are gray colored.

The $J(A)$ maps were paired with the complete data set $Pf(all)$ then compared using a bootstrap paired t-test (library *MKinfer* in R) as a two-sample test with unequal variances and paired samples. For the ENSO data, we compared $Pf(A)$ with $Pf(Neutral)$. The test was done pairwise as each pixel (or location) is considered twice, once in the $J(A)$ and once in $Pf(all)$. The null hypothesis was that $Pf(all)$ and each $J(A)$ have the same mean, which translates to the absence of difference between the means of the full data set and the jackknife map. As the maps of the HG contain a large number of pixels (90,630 pixels), the maps were assumed to follow a normal distribution. The results from each t-test (Student *t*, mean difference, *p*-value, confidence interval from the t-test) are summarized in Table 1. General statistics were also generated including the mean, standard deviation as well as minimum, first and third quantiles (noted as "*first Q*" and "*third Q*" in the table), median and maximum (Table 1). The degree of freedom (50,170) was identical throughout every factor as we restricted analysis to pixels present in every map (i.e., no missing values).

This approach is based on a pixel-by-pixel analysis and only gives information on the general contribution of a variable (Levine et al., 2009). To visualize how each factor impacted the spatial distribution of fronts, we plotted spatial changes by selectively isolating the extreme values of every $\delta(A)$ below the 12.5th percentile and above the 87.5th percentile in a $64 * 64$ window. Because of how these δ variables were constructed, the minimum δ values correspond to the areas where the $J(A)$ values are also the smallest (i.e., where each factor has maximum impact), and vice versa. Hence, the value of δ were multiplied by -1 to facilitate interpretation. For example, in Figure 5d, a high value of $-\delta$ in the area of Kawau means there is a higher frontal presence there in summer.

Average maps of near-surface chlorophyll (CHL) were compiled for each group (dominant wind, season, and ENSO phase) to provide insight on what kind of water masses the identified fronts might be separating.

3. Results

3.1. General Frontal Probability and Properties

Tīkapa Moana Te Moananui ā Toi HG channels and near-shore regions (Figure 3) are characterized by higher frontal probabilities with hotspots north of Aotea (36°S, 175.45°E; $Pf \approx 5\%$), around Cape Colville (36.5°S−175.25°E; $Pf \approx 3.5\%$), North of Kawau (36.4°S−174.7°E; $Pf \approx 5\%$), West of Whanganui (36.75°S−175.45°E; $Pf \approx 3.5\%$), north of Waiheke, and in the Firth of Tames (37.2°S−175.4°E; $Pf \approx 4.5\%$). Three lines of higher probabilities stand out, one between Kawau and Waiheke ($Pf \approx 3.5\%$), the second originating from Cape Colville to Kawau ($Pf \approx 3\%$), and lastly a weaker one between Cape Colville and Waiheke ($Pf \approx 2.5\%$). These sets of fronts effectively structure the gulf in three sections, one being the Firth of Thames, another in the triangle Waiheke-

Kawau-Cape Colville usually referred to as the inner gulf (Gaskin, 2021) and the last one North of the line Kawau-Cape Colville usually identified as outer gulf (Gaskin, 2021).

3.2. Spatio-Temporal Variability

All results presented in Figures 4, 5, and 7 are paired showing the probability of a factor (e.g., spring, Figure 5a) and the associated $-\delta$ (e.g., spring, Figure 5b).

3.2.1. Wind Direction

Out of the eight wind directions considered for the analysis, only four are detailed here. The first two are North-West (NW, Figures 4a and 4b) and South-East (SE, Figures 4c and 4d) as these are expected to promote upwelling (NW) and downwelling (SE) (Zeldis et al., 2004). The other wind origins we considered are West (Figures 4e and 4f) and East (Figures 4g and 4h) as they both have components close to the NW-SE axis, and are more frequent than meridional winds (Table S1 in Supporting Information S1).

Dominant NW winds (Figures 4a and 4b) correspond to increases in frontal probability in the center of the inner and outer Gulf, as well as across the Jellicoe and Cradock channels, likely separating Gulf waters from oceanic waters characterized by lower CHL values (Figure S2a in Supporting Information S1). North of Aotea and north of Kawau are two areas that show important patches of decreased probability. This wind origin is evaluated non-significant by the Student t-test result (Table 1) and the values of the jackknife are of smaller magnitude compared to other wind origins with higher occurrences. For example, NW winds $-\delta$ range from -0.45% to 0.29% while westerlies $-\delta$ range from -0.69% to 1.5%. When SE winds dominate (Figures 4c and 4d), frontal probability increases along the 40 m isobath, off of Colville Cape toward Kawau, across the Cradock channel and north of Te-Hauturu (which displays generally higher CHL values compared to other wind directions, Figure S2 in Supporting Information S1). Small patches of decreased probability are present off the coast of Pakiri and in the center of the inner-Gulf. The impact of SE winds is identified as significant under the bootstrap Student t-test. Westerlies (Figures 4e and 4f) create important decreases along the 40 and 70 m isobath and a strong increase from Pakiri into the inner Gulf by the Jellicoe channel. Westerlies are significant as well in the bootstrap t-test. Easterlies winds (Figures 4g and 4h) show increased probability on a line between Kawau and Cape Colville, and between the 70 and 100 m isobath north of Te-Hauturu-ō-Toi. Areas of decreased probability are noticeable by Pakiri, in the Cradock channel and north of the Mokohinau islands. Easterlies are significant on the bootstrap t-test.

3.2.2. Seasons

In spring, frontal probability decreases inside the inner Gulf as well as along the 100 m isobath compared to other seasons (Figures 5a and 5b). This is consistent with the relatively uniform CHL average values for this season within the HG (Figure 6a). Local increases are observed in four areas of the outer Gulf: Jellicoe and Cradock channels, north of Waiheke and Cape Colville. The Cradock channel in particular might host fronts separating high CHL waters from the Pakiri and Kawau region (possibly fertilized by upwelling) from lower-CHL oceanic waters (Figure 6a). A general increase is visible offshore past the 100 m isobath where oceanic waters encounter HG waters in spring (Figure 6a). This season is significant in the bootstrap t-test. In summer (Figures 5c and 5d) frontal probability is patchy on the 70 m isobath and beyond, with numerous patches of increased and decreased probability. Probability increases around Kawau, north Waiheke and Cape Colville show greater intensity than in spring. This is reflected in an approaching to the coast of low CHL waters (Figure 6b). Summer is also significant in the bootstrap t-test. In autumn (Figures 5e and 5f) high front probability areas shift to follow the 40 m isobath and flow from Kawau out to the Colville channel. Out of the Gulf, high probabilities are mostly present between the 70 and 100 m isobath corresponding to a movement toward offshore of low CHL waters (Figure 6c). Past the 100 m isobath, important decreases start to show-up, as well as in the Cradock channel, around Cape Colville and near Pakiri. This season is however non-significant in the bootstrap Student t-test result (Table 1). Winter (Figures 5g and 5h) is characterized by massive decrease in frontal probability all over the study area, and it is especially noticeable around Kawau, north of Waiheke, Whanganui and Cape Colville, mirroring summer. We also observe a more subtle general decrease past the 100 m isobath as the change in CHL values appear more gradual from the near-shore toward the oceanic low CHL waters (Figure 6d). Two increases strands can be seen in the inner Gulf and between the 70 and 100 m isobath (like in autumn), and a weaker increase line following the 100 m isobath. Winter turns out significant in the bootstrap t-test.

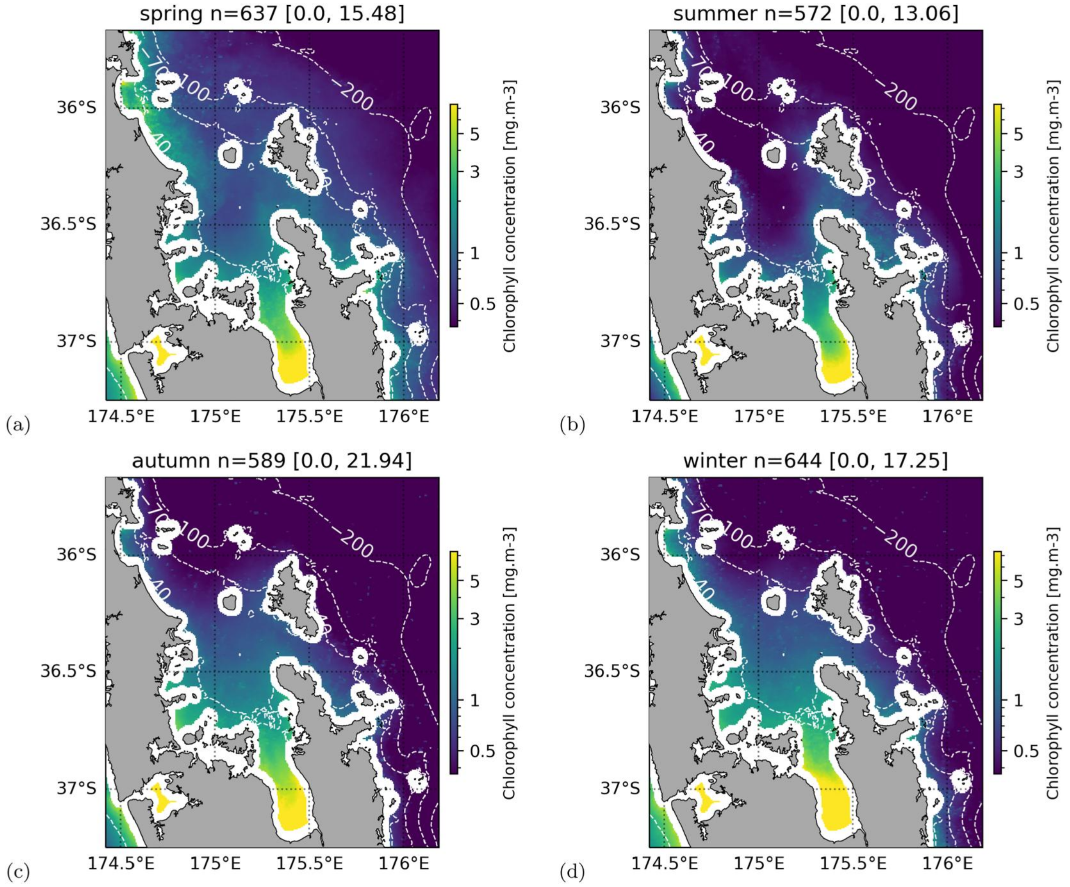

Figure 6. Chlorophyll concentration maps during seasons, top to bottom: spring (a), summer (b), autumn (c), winter (d). Dashed lines indicate 40, 70, 100, and 200 m depth. The title of each sub-figure indicates the factor, *n* the number of days and the min and max values. Note logarithmic scale.

3.2.3. ENSO

Based on the SOI index, there were two *El Niño* periods and one *La Niña* during the 6.5 years covered by this study. The two *El Niño* events occurred from May 2016 to August 2016 and from June 2019 to March 2020. As for the *La Niña* event, it occurred from December 2020 to December 2022.

The spatial distributions of average chlorophyll concentrations during the different ENSO phases are relatively similar (Figure S3 in Supporting Information S1). The only noticeable difference is the appearance of a patch of low CHL north of Te-Hauturu-ō-Toi during the *Neutral* phase of ENSO (Figure S3b in Supporting Information S1).

Yet, frontal composites reveal measurable differences: during *El Niño* periods (Figures 7a and 7b), lines of increased probability can be seen at the 40 m isobath separating the Firth of Thames and the inner Gulf, and east of Kawau separating the inner Gulf and outer Gulf. Additionally, increases in frontal probability are noticeable between the north of Pakiri's coast and the Mokohinau islands, and NW of Aotea. There are also noticeable decreases in the center of the inner Gulf and on Pakiri's coastline.

During *La Niña* events (Figures 7c and 7d), higher values of frontal probabilities along the 40 m isobath persisted, separating the Firth of Thames and the inner Gulf. However, the eastern line from Kawau is replaced by a southern one toward Waiheke, promoting horizontal exchanges between the inner and outer Gulf. The line of fronts previously observed between the north of Pakiri's coast and the Mokohinau islands moved toward 70 m isobath, and a second increased probability line appear parallel to the first, north of the Mokohinau islands.

Both *El Niño* and *La Niña* events are significant under the bootstrap t-test.

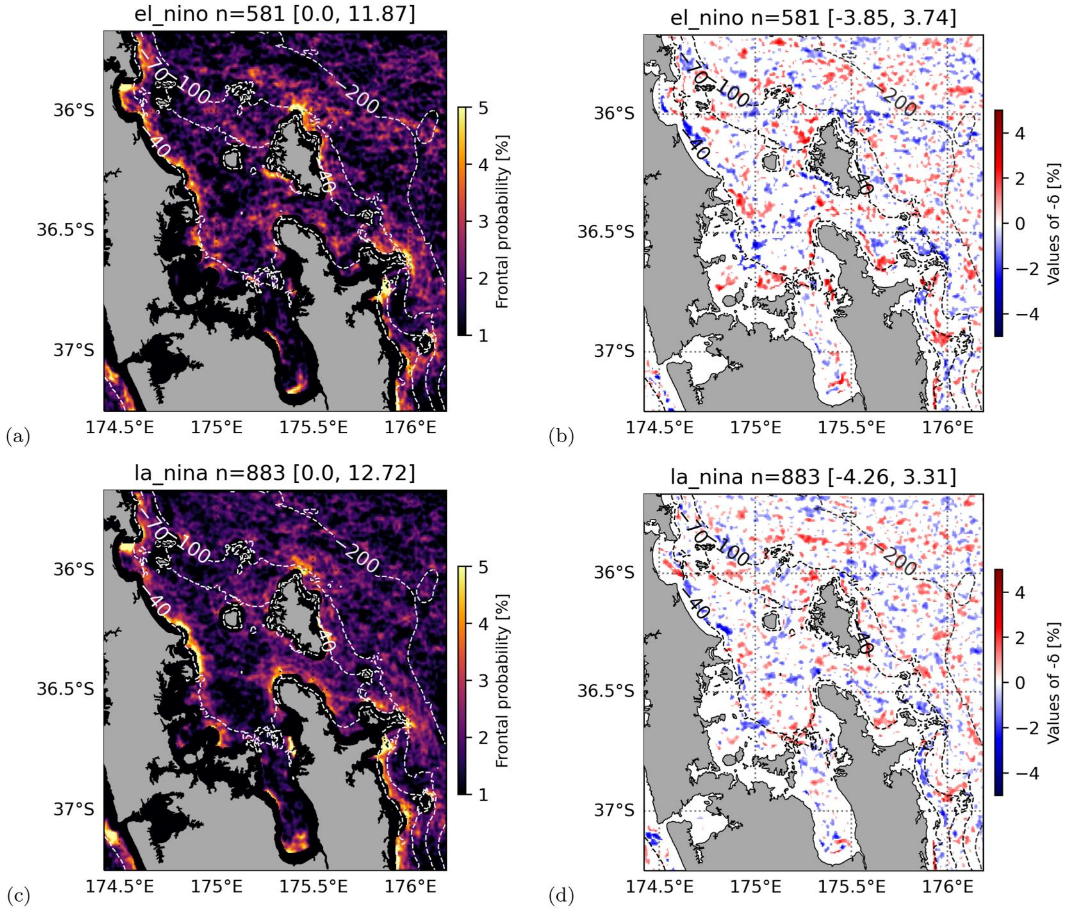

Figure 7. Probability maps and values of $-\delta$ outside of the 75th percentile confidence interval during El Niño Southern Oscillation phases, top to bottom: *El Niño* (a, b), *La Niña* (c, d). Probabilities are on the left column (a, c) and δ on the right. Dashed line indicates 40, 70, 100, and 200 m depth. The title of each sub-figure indicates the factor, n the number of days and the min and max values. Note the change of scale in δ.

4. Discussion

Frontal probabilities in the Tīkapa Moana Te Moananui ā Toi HG are highest along the coast and in the middle of the outer-Gulf between Kawau, Waiheke and the Colville Cape (Figure 3). Our results indicate that the distribution of fine-scale surface fronts is modulated by winds, seasons, and ENSO phases. Across all studied parameters (wind, season, ENSO), higher frontal probability patches in the HG overlap with the 70 and 40 m isobaths. The distribution of fronts tends to separate HG in three distinct sub-regions, corresponding to what has been identified in the literature as the outer-Gulf, inner-Gulf, and Firth of Thames respectively. More precisely, the Firth of Thames to inner Gulf separation is facilitated by fronts following the 40 m isobath, while fronts between Kawau and Cape Colville following the 70 m isobath separate the waters of the inner and outer gulf. Gaskin (2021) roughly follow the same isobath though they use Cape Rodney (between Pakiri and Kawau) to Cape Colville as the limit between inner and outer Gulf. In general, the outer Gulf tends to be impacted by oceanic inputs and is characterized by saltier, clearer, and warmer waters (Zeldis et al., 2004) compared to the inner Gulf where rainfall and river inputs are important drivers of water properties and productivity (Zeldis & Willis, 2015). These sub-regions are not isolated from each other but the exchanges of water between them are modulated by the presence and orientation of frontal features. For example, when a front is parallel to the 70 m isobath, separating the inner and outer Gulf, we expect a limitation of the exchanges between the two, whereas, when fronts are not parallel to the 70 m isobath, we expect such exchanges to be promoted (Gangrade & Franks, 2023).

To correctly interpret the observed patterns, we need to account for the intricacies of ocean color and the statistical approaches we used in our analysis. Isolating the sediment from chlorophyll is a key element of OLCI data set processing, yet Blondeau-Patissier et al. (2014) showed that none of the current algorithms are able to properly remove the sediment signal, which will in turn impact the front detection results using OLCI. The only processing in removing the sediment signal was done prior to download by the OC4ME algorithm from the Copernicus Marine Service (EUMETSAT, 2021). We also removed values of CHL above 30 $mg.m^{-3}$, considering that OC4ME tend to overestimate values above this value (EUMETSAT, 2021). Hence, it is likely that at least some of the coastal fronts results from gradients in sediment concentration (e.g., associated with increase rainfall and river outflows) rather that gradients in chlorophyll, especially in the Firth of Thames (O'Callaghan & Stevens, 2017). However, these regions highlighted at hotspots of frontal activities, would still represent regions where water masses of different optical properties converge. If in one of the sides of the front the ocean color signal is heavily dominated by sediments, we expect that the waters therein would likely have very different biological properties compared to the clearer waters brought nearby by the frontal circulation, even if this difference is not measured in terms of chlorophyll (Miller, 2004; Shutler et al., 2010). Very high values of probability directly next to the shore are due to the sensibility of the algorithm which enables us to detect fronts in the highly dynamic coastal environment. Using remotely sensed ocean color also introduces a bias: our results are reflective of cloud-free days. Cloudy days might display different patterns that cannot be captured by our approach. In situ studies are required to complement our approach.

As for statistics, the size of the data set has a strong impact on the number of degree of freedom (here 50,170) because we considered each pixel as an observation. Attempts at correcting this DoF inflation by bootstrapping and manually reducing the DoF showed little to no impact, most changes in p-value being close to 10^{-5} or lower. Hence, we edited the method of Levine et al. (2009) by using a bootstrapped Student test instead of a normal one, to be as robust in the analysis as possible.

Because of our working hypothesis being that biologically important fronts are characterized by strong chlorophyll gradient as depicted by Lévy et al. (2018), we chose to use a gradient-based front detection algorithm as the core calculation of the pyBOA. The original BOA was developed by Belkin and O'Reilly (2009), and later used by Galuardi (2012) and Lin et al. (2019), precisely to deal with strong chlorophyll gradients created by the *slope-shelf* effect (Belkin & O'Reilly, 2009). The presence of the shelf and slope nearby highly influence the circulation in HG (Stevens et al., 2021; Zeldis et al., 2004). Our results are consistent with this view showing an overlap of fronts with the 100 m isobath, in addition to others more related to the bathymetry than the shelf (40, 70 m). This shelf effect is documented in other parts of Aotearoa New Zealand such as around the Otago shelf (Hopkins et al., 2010).

The frontal probabilities movements also relate to changes in wind direction throughout the seasons, with westerlies in winter and spring, switching to easterlies in summer and autumn. This cycle explains the nearshore-offshore oscillation in fronts position displayed in Figure 5 between winter-spring and summer-autumn and is related to changes in average CHL concentration (Figure 6) and to shifts in plankton distribution (Chang et al., 2003; Jillett, 1971; Sharples, 1997). The oscillation observed in HG is similar to the observation of Hopkins et al. (2010), showing the South Tropical Front close to shore in summer-autumn and further offshore during winter-spring. This similarity may originate from the similarity of bathymetry, both areas having a strong shelf break (Hopkins et al., 2010; Zeldis et al., 2004). In addition, the switch to easterlies in *La Niña* periods (Zeldis et al., 2004) explains why some of the fronts observed seem pushed into the Gulf by comparison to *Neutral* ENSO phase. A shift in average CHL concentration is not evident in our results (Figure S3 in Supporting Information S1), suggesting that these fronts have a different structure across different seasons. Future work, ideally complemented by in situ measurements, is required to disentangle the effects of seasonality and ENSO phases combined.

The effects of tides on the movement of fronts are not approached in this study. However, Hu et al. (2016) suggest that tides are important factor in fine-scale structure movement, sometimes moving sediment fronts up to 10 km. While in our study it was not possible to address this issue due to data availability (one image per day), we suspect the tides can shift the position of fronts across the Gulf. Multiple images throughout the day on a similar resolution would allow future description of the tidal effect in our study area.

Fronts are associated with enhanced productivity (Lévy et al., 2018; McGillicuddy, 2016) regardless of the scale considered. This boosted productivity and altered conditions are important feeding grounds used by megafauna (Braun et al., 2019; Snyder et al., 2017) and the fishing industry alike (Watson et al., 2018). Spatial shifts in frontal distribution associated to changes in seasons may therefore displace hotspots of productivity across the HG, potentially driving the movement of aggregations of seabirds (Gaskin, 2021) or overwintering cetaceans (Gostischa et al., 2021; Izadi et al., 2022). In addition, seasonal variations of frontal locations can impact the dispersal of planktonic larvae from sessile species with different spawning times (Michie, 2023). For example, crayfish mating period in winter (Kelly, 2001; MacDiarmid, 1989) matches with increase frontal probability in the inner Gulf contributing to their dispersion or retention.

On a larger scale, looking at the effect of the ENSO phases, it appears that the shift from one phase to another (e.g., *El Niño* to *La Niña*) has major impact of seabirds (Gaskin, 2021). While the effects of ENSO only account for part of the interannual variability for temperature and rainfall (25% in Gaskin (2021)), the wind effects have been suggested to be more significant. Stronger westerlies typical of *El Niño* could mitigate the general shift in wind direction in summers towards easterly winds, with the potential of decreasing oceanic intrusions in the HG and changing the distribution of fronts between water masses of oceanic and coastal origins. Gaskin (2021) measured a drop in seabirds weight after each shift from *El Niño* to *La Niña* and hypothesized that this trend is linked with shifts in their zooplanktonic and fish prey quality and distribution. Our observations suggest that the transition from *El Niño* to *La Niña* results at least in shifts in frontal distribution which might change the distribution of prey items for megafauna, including wintering marine mammals (Gostischa et al., 2021; Hamilton, 2020), and commercially important species such as tuna, which have been observed to forage on fronts (Snyder et al., 2017).

The Gulf segmentation into three regions has been suggested by previous studies (Chang et al., 2003; Gaskin, 2021; Zeldis et al., 2004). Although fronts tend to separate these three regions which are influenced by different drivers (e.g., oceanic waters in the outer Gulf, land input in the Firth of Thames (Gaskin, 2021)), they still exchange water parcels. For example, the Firth of Thames and Inner Gulf are separated by an area of high frontal frequency. Nevertheless, exchanges between these two regions are still reflected in the similarity of water masses therein between July and August 2012 (O'Callaghan & Stevens, 2017). Yet, this similarity was not present in their 2013 data possibly because of a shift from *La Niña* to *Neutral* ENSO conditions. The oceanic input can be seen not only in the outer Gulf but also in the inner Gulf especially in summer-autumn (Figure 6). This observation is consistent with Paul (1968) Study of surface level temperature. Exchanges between the inner and outer Gulf, both observed through frontal presence here and other biological (Chang et al., 2003; Jillett, 1971) or physical (Paul, 1968) variables in the literature, are modulated by wind shifts and underwater topography interactions. The chlorophyll repartition observed in this study (Figure 6, Figures S2 and S3 in Supporting Information S1) show that different environmental drivers (e.g., winds, season, ENSO) affect the CHL content at the surface. Typically, easterlies are associated with lower chlorophyll concentrations, as they push the oceanic waters of the EAuC near shore (Zeldis et al., 2004). This is especially visible in summer-autumn (Figures 6b and 6c), where the EAuC intrusion brings low CHL water all the way into the inner Gulf.

5. Conclusion

This study compiled a first map of frontal probabilities for the HG by customizing an existing algorithm in order to detect fine-scale fronts from OLCI. We successfully used a gradient approach to reliably identify fronts and characterize the frontal patterns both spatially and temporally. We show that the fronts in the HG follow specific seasonal and ENSO patterns, governed by the bathymetry and winds. Wind effects are especially visible for the Southwesteries, Westerlies and Easterlies, and through a seasonal shift of wind direction (easterlies dominate in summer-autumn, westerlies in winter-spring) resulting in frontal movements across the Gulf. ENSO modulates the connectivity and separation between the inner and outer Gulf, “closing” during *El Niño* and “opening” during *La Niña*. In addition, the separation of the Gulf in three different subregions is proven coherent from a frontal perspective as fronts along the 40 and 70 m isobath contribute to this separation.

Data Availability Statement

The wind data set used in this article was provided by the Meteorological Service of New Zealand Ltd, covering the stations of Mokohinau. This data set is only available through Meteorological Service of New Zealand Ltd. To access it, please contact Neal Osborn (Neal.Osborne@metservice.com). The SOI index data set was gathered from https://psl.noaa.gov/gcos_wgsp/Timeseries/Data/soi.long.data (NOAA, 2022). The satellite data used for the detection are provided by Copernicus Marine Services (Copernicus, 2016), see https://doi.org/10.48670/moi-

00280. All maps presented here are made using python 3.9 *cartopy* package (Met Office, 2010–2015). The pyBOA 1.0.0 is freely available: https://doi.org/10.5281/zenodo.8135921 (Lhériau-Nice, 2023). This version of the algorithm was build using python 3.9 with Anaconda3 2022.05.

The data set from ERA5 used for the supplementary materials were downloaded from https://cds.climate.copernicus.eu/cdsapp#!/dataset/reanalysis-era5-single-levels?tab=overview (Hersbach et al., 2023).

Acronyms

BOA:	Belkin and O'Reilly Algorithm
CHL:	Chlorophyll-a
DoF:	Degree of Freedom
EAuC:	East Auckland Current
ENSO:	El Niño Southern Oscillation
OLCI:	Ocean-Land Color Instrument
SOI:	Southern Oscillation Index
HG:	Tīkapa Moana Te Moananui ā Toi Hauraki Gulf

Acknowledgments

Our thanks go to Dr. Igor Belkin, Dr. Lei Lin and Dr. Benjamin Galuardi for answering our questions about transferring the code to python and providing their own code in MATLAB/R-core. We also thank the statistical services to the University of Auckland for their advice and review of the methods. We thank Pr. Andrew Jeffs for supporting this project. This work was supported by the University of Auckland via the Faculty Research Development Fund (Grant 3724591) and the Departmental Performance Based Research Funding (PBRF). We are thankful for the constructive feedback of the reviewers, allowing for a better quality of the manuscript. Open access publishing facilitated by The University of Auckland, as part of the Wiley - The University of Auckland agreement via the Council of Australian University Librarians.

References

Auckland Council. (2021). The hapū and iwi of Tāmaki Makaurau. Retrieved from http://www.aucklandcouncil.govt.nz/plans-projects-policies-reports-bylaws/our-plans-strategies/auckland-plan/about-the-auckland-plan/Pages/iwi-tamaki-makaurau.aspx

Belkin, I. M., & O'Reilly, J. E. (2009). An algorithm for oceanic front detection in chlorophyll and SST satellite imagery. *Journal of Marine Systems*, *78*(3), 319–326. https://doi.org/10.1016/j.jmarsys.2008.11.018

Blondeau-Patissier, D., Gower, J. F. R., Dekker, A. G., Phinn, S. R., & Brando, V. E. (2014). A review of ocean color remote sensing methods and statistical techniques for the detection, mapping and analysis of phytoplankton blooms in coastal and open oceans. *Progress in Oceanography*, *123*, 123–144. https://doi.org/10.1016/j.pocean.2013.12.008

Braun, C. D., Gaube, P., Sinclair-Taylor, T. H., Skomal, G. B., & Thorrold, S. R. (2019). Mesoscale eddies release pelagic sharks from thermal constraints to foraging in the ocean twilight zone. *Proceedings of the National Academy of Sciences*, *116*(35), 17187–17192. https://doi.org/10.1073/pnas.1903067116

Cayula, J.-F., & Cornillon, P. (1992). Edge detection algorithm for SST images. *Journal of Atmospheric and Oceanic Technology*, *9*(1), 67–80. https://doi.org/10.1175/1520-0426(1992)009⟨0067:EDAFSI⟩2.0.CO;2

Chang, F. H., Zeldis, J., Gall, M., & Hall, J. (2003). Seasonal and spatial variation of phytoplankton assemblages, biomass and cell size from spring to summer across the north-eastern New Zealand continental shelf. *Journal of Plankton Research*, *25*(7), 737–758. https://doi.org/10.1093/plankt/25.7.737

Chiswell, S. M., Gutiérrez-Rodríguez, A., Gall, M., Safi, K., Strzepek, R., Décima, M. R., & Nodder, S. D. (2022). Seasonal cycles of phytoplankton and net primary production from Biogeochemical Argo float data in the south-west Pacific Ocean. *Deep-Sea Research Part I: Oceanographic Research*, *187*, 103834. https://doi.org/10.1016/j.dsr.2022.103834

Colella, S., Böhm, E., Cesarini, C., Garnesson, P., Netting, J., & Calton, B. (2022). *Product user manual for ocean colour products OCEANCOLOUR_glo_bgc_l3_nrt_009_101 OCEANCOLOUR_glo_bgc_l4_nrt_009_102 OCEANCOLOUR_glo_bgc_l3_my_009_103 OCEANCOLOUR_glo_bgc_l4_my_009_104 OCEANCOLOUR_glo_bgc_l3_my_009_107 OCEANCOLOUR_glo_bgc_l4_my_009_108 OCEANCOLOUR_atl_bgc_l3_nrt_009_111 OCEANCOLOUR_atl_bgc_l4_nrt_009_112 OCEANCOLOUR_atl_bgc_l3_my_009_113 OCEANCOLOUR_atl_bgc_l4_my_009_114 OCEANCOLOUR_atl_bgc_l4_nrt_009_116 OCEANCOLOUR_atl_bgc_l4_my_009_118 OCEANCOLOUR_arc_bgc_l3_nrt_009_121 OCEANCOLOUR_arc_bgc_l4_nrt_009_122 OCEANCOLOUR_arc_bgc_l3_nrt_009_123 OCEANCOLOUR_arc_bgc_l4_nrt_009_124 OCEANCOLOUR_bal_bgc_l3_nrt_009_131 OCEANCOLOUR_bal_bgc_l4_nrt_009_132 OCEANCOLOUR_bal_bgc_l3_my_009_133 OCEANCOLOUR_med_bgc_l3_nrt_009_141 OCEANCOLOUR_med_bgc_l4_nrt_009_142 OCEANCOLOUR_med_bgc_l3_my_009_143 OCEANCOLOUR_med_bgc_l4_my_009_144 OCEANCOLOUR_blk_bgc_l3_nrt_009_151 OCEANCOLOUR_blk_bgc_l4_nrt_009_152 OCEANCOLOUR_blk_bgc_l3_my_009_153 OCEANCOLOUR_blk_bgc_l4_my_009_154 Issue: 1.0* (Tech. Rep.). European Organisation for the Exploitation of Meteorological Satellites. Retrieved from https://catalogue.marine.copernicus.eu/documents/PUM/CMEMS-OC-PUM.pdf

Copernicus. (2016). Global ocean colour (Copernicus-GlobColour), Bio-Geo-Chemical, L3 (daily) from Satellite Observations (1997-ongoing) [Dataset]. https://doi.org/10.48670/moi-00280

EUMETSAT. (2021). *Sentinel-3 product notice – OLCI Level-2 ocean colour* (Tech. Rep.). European Organisation for the Exploitation of Meteorological Satellites. Retrieved from https://articlereview.pubmate.in/#/?templateID=a9e4e0b303ea4b148548862492174aa5060420502

Galuardi, B. (2012). boaR-package: The Belkin-O'Reilly front detection algorithm [Software]. Retrieved from https://rdrr.io/github/galuardi/boaR/man/boaR-package.html

Gangrade, S., & Franks, P. J. S. (2023). Phytoplankton patches at oceanic fronts are linked to coastal upwelling pulses: Observations and implications in the California Current System. *Journal of Geophysical Research: Oceans*, *128*(3), e2022JC019095. https://doi.org/10.1029/2022JC019095

Gaskin, C. (2021). *State of our Seabirds 2021 - Seabird ecology, research and conservation for the wider Hauraki Gulf/Tīkapa Moana/Te Moananui-ā-Toi region* (Tech. Rep.). Northern New Zealand Seabirds Charitable Trust.

Gostischa, J., Massolo, A., & Constantine, R. (2021). Multi-species feeding association dynamics driven by a large generalist predator. *Frontiers in Marine Science*, *8*, 739894. https://doi.org/10.3389/fmars.2021.739894

Hamilton, O. (2020). The ecology of large marine predators in the Hauraki Gulf (Thesis, ResearchSpace@Auckland). Retrieved from https://researchspace.auckland.ac.nz/handle/2292/56694. (Accepted: 2021-09-29T02:34:34Z).

Hersbach, H., Bell, B., Berrisford, P., Biavati, G., Horányi, A., Muñoz Sabater, J., et al. (2023). ERA5 hourly data on single levels from 1940 to present [Dataset]. https://doi.org/10.24381/cds.adbb2d47

Hopkins, J., Shaw, A., & Challenor, P. (2010). The Southland Front, New Zealand: Variability and ENSO correlations. *Continental Shelf Research*, *30*(14), 1535–1548. https://doi.org/10.1016/j.csr.2010.05.016

Hu, Z., Pan, D., He, X., & Bai, Y. (2016). Diurnal variability of turbidity fronts observed by geostationary satellite ocean color remote sensing. *Remote Sensing*, *8*(2), 147. https://doi.org/10.3390/rs8020147

Izadi, S., Aguilar de Soto, N., Constantine, R., & Johnson, M. (2022). Feeding tactics of resident Bryde's whales in New Zealand. *Marine Mammal Science*, *38*(3), 1104–1117. https://doi.org/10.1111/mms.12918

Jillett, J. B. (1971). Zooplankton and hydrology of Hauraki Gulf, New Zealand. Retrieved from http://archive.org/details/nzoimemoir00531971

Kelly, S. (2001). Temporal variation in the movement of the spiny lobster *Jasus edwardsii*. *Marine and Freshwater Research*, *52*(3), 323. https://doi.org/10.1071/MF00028

Lehahn, Y., d'Ovidio, F., Lévy, M., & Heifetz, E. (2007). Stirring of the northeast Atlantic spring bloom: A Lagrangian analysis based on multisatellite data. *Journal of Geophysical Research*, *112*, C08005. https://doi.org/10.1029/2006JC003927

Levine, R. S., Yorita, K. L., Walsh, M. C., & Reynolds, M. G. (2009). A method for statistically comparing spatial distribution maps. *International Journal of Health Geographics*, *8*(1), 7. https://doi.org/10.1186/1476-072X-8-7

Lhériau-Nice, A. (2023). pyBOA: Contextual front detection [Software]. https://doi.org/10.5281/zenodo.8135921

Lin, L., Liu, D., Luo, C., & Xie, L. (2019). Double fronts in the Yellow Sea in summertime identified using sea surface temperature data of multi-scale ultra-high resolution analysis. *Continental Shelf Research*, *175*, 76–86. https://doi.org/10.1016/j.csr.2019.02.004

Liu, X., & Levine, N. M. (2016). Enhancement of phytoplankton chlorophyll by submesoscale frontal dynamics in the North Pacific Subtropical Gyre. *Geophysical Research Letters*, *43*(4), 1651–1659. https://doi.org/10.1002/2015GL066996

Lévy, M., Ferrari, R., Franks, P. J. S., Martin, A. P., & Rivière, P. (2012). Bringing physics to life at the submesoscale. *Geophysical Research Letters*, *39*, L14602. https://doi.org/10.1029/2012GL052756

Lévy, M., Franks, P. J. S., & Smith, K. S. (2018). The role of submesoscale currents in structuring marine ecosystems. *Nature Communications*, *9*(1), 4758. https://doi.org/10.1038/s41467-018-07059-3

MacDiarmid, A. B. (1989). Moulting and reproduction of the spiny lobster *Jasus edwardsii* (Decapoda: Palinuridae) in northern New Zealand. *Marine Biology*, *103*(3), 303–310. https://doi.org/10.1007/BF00397263

Mahadevan, A. (2016). The impact of submesoscale physics on primary productivity of plankton. *Annual Review of Marine Science*, *8*(1), 161–184. https://doi.org/10.1146/annurev-marine-010814-015912

Mangolte, I., Lévy, M., Haëck, C., & Ohman, M. D. (2023). Sub-frontal niches of plankton communities driven by transport and trophic interactions at ocean fronts (Preprint). *Biogeophysics: Physical - Biological Coupling*. https://doi.org/10.5194/egusphere-2023-471

Mauzole, Y., Torres, H., & Fu, L. (2020). Patterns and dynamics of SST fronts in the California Current System. *Journal of Geophysical Research: Oceans*, *125*(2), e2019JC015499. https://doi.org/10.1029/2019JC015499

McGillicuddy, D. J. (2016). Mechanisms of physical-biological-biogeochemical interaction at the oceanic mesoscale. *Annual Review of Marine Science*, *8*(1), 125–159. https://doi.org/10.1146/annurev-marine-010814-015606

Met Office. (2010–2015). Cartopy: A cartographic Python library with a matplotlib interface [Software]. Exeter, Devon. Retrieved from https://scitools.org.uk/cartopy

Michie, C. A. G. (2023). Variation in larval dispersal patterns and its power in predicting genetic divergence of benthic marine invertebrates around New Zealand (Unpublished doctoral dissertation). ResearchSpace@ Auckland.

Miller, P. (2004). Multi-spectral front maps for automatic detection of ocean colour features from SeaWiFS. *International Journal of Remote Sensing*, *25*(7–8), 1437–1442. https://doi.org/10.1080/01431160310001592409

NOAA. (2022). SOI indices 1951-current time [Dataset]. Retrieved from https://psl.noaa.gov/gcos_wgsp/Timeseries/Data/soi.long.data

O'Callaghan, J. M., & Stevens, C. L. (2017). Evaluating the surface response of discharge events in a New Zealand Gulf-ROFI. *Frontiers in Marine Science*, *4*, 232. https://doi.org/10.3389/fmars.2017.00232

Palter, J. B. (2015). The role of the Gulf Stream in European Climate. *Annual Review of Marine Science*, *7*(1), 113–137. https://doi.org/10.1146/annurev-marine-010814-015656

Paul, L. J. (1968). Some seasonal water temperature patterns in the Hauraki Gulf, New Zealand. *New Zealand Journal of Marine and Freshwater Research*, *2*(3), 535–558. https://doi.org/10.1080/00288330.1968.9515254

Ridgway, K., & Hill, K. (2009). In E. S. Poloczanska, A. J. Hobday, & A. J. Richardson (Eds.), *The East Australian current*. NCCARF Publication. Retrieved from https://nora.nerc.ac.uk/id/eprint/528665/

Sharples, J. (1997). Cross-shelf intrusion of subtropical water into the coastal zone of northeast New Zealand. *Continental Shelf Research*, *17*(7), 835–857. https://doi.org/10.1016/S0278-4343(96)00060-X

Shutler, J. D., Grant, M. G., Miller, P. I., Rushton, E., & Anderson, K. (2010). Coccolithophore bloom detection in the north east Atlantic using SeaWiFS: Algorithm description, application and sensitivity analysis. *Remote Sensing of Environment*, *114*(5), 1008–1016. https://doi.org/10.1016/j.rse.2009.12.024

Smith, W. L., Rao, P. K., Koffler, R., & Curtis, W. R. (1970). The determination of sea-surface temperature from satellite high resolution infrared window radiation measurements. *Monthly Weather Review*, *98*(8), 604–611. https://doi.org/10.1175/1520-0493(1970)098⟨0604:TDOSST⟩2.3.CO;2

Snyder, S., Franks, P. J. S., Talley, L. D., Xu, Y., & Kohin, S. (2017). Crossing the line: Tunas actively exploit submesoscale fronts to enhance foraging success. *Limnology and Oceanography Letters*, *2*(5), 187–194. https://doi.org/10.1002/lol2.10049

Stevens, C. L., O'Callaghan, J. M., Chiswell, S. M., & Hadfield, M. G. (2021). Physical oceanography of New Zealand/Aotearoa shelf seas – A review. *New Zealand Journal of Marine and Freshwater Research*, *55*(1), 6–45. https://doi.org/10.1080/00288330.2019.1588746

Su, J. & Pu, Y. X. (1987). The Kuroshio. *Endeavour*, *11*(3), 137–142. https://doi.org/10.1016/0160-9327(87)90202-x

Thomas, L. N., Tandon, A., & Mahadevan, A. (2008). Submesoscale processes and dynamics. In M. W. Hecht & H. Hasumi (Eds.), *Geophysical monograph series* (Vol. 177, pp. 17–38). American Geophysical Union. https://doi.org/10.1029/177GM04

Watson, J. R., Fuller, E. C., Castruccio, F. S., & Samhouri, J. F. (2018). Fishermen follow fine-scale physical ocean features for finance. *Frontiers in Marine Science*, *5*, 46. https://doi.org/10.3389/fmars.2018.00046

Zeldis, J. R., & Willis, K. (2015). Biogeographic and trophic drivers of mesozooplankton distribution on the northeast continental shelf and in Hauraki Gulf, New Zealand. *New Zealand Journal of Marine and Freshwater Research*, *49*(1), 69–86. https://doi.org/10.1080/00288330.2014.955806

Zeldis, J. R., Walters, R. A., Greig, M. J. N., & Image, K. (2004). Circulation over the northeastern New Zealand continental slope, shelf and adjacent Hauraki Gulf, during spring and summer. *Continental Shelf Research*, *24*(4), 543–561. https://doi.org/10.1016/j.csr.2003.11.007

Erratum

The originally published version of this article contained a typographical error. The term “Tīpaka Moana” throughout should be “Tīkapa Moana.” The error has been corrected, and this may be considered the authoritative version of record.